







Spin-polarized oxygen evolution reaction under magnetic field

Xiao Ren^{1,2}, Tianze Wu ^{1,2,3}, Yuanmiao Sun², Yan Li¹, Guoyu Xian¹, Xianhu Liu ⁴, Chengmin Shen¹, Jose Gracia ⁵, Hong-Jun Gao ¹, Haitao Yang ¹✉ & Zhichuan J. Xu ^{2,3,6}✉

The oxygen evolution reaction (OER) is the bottleneck that limits the energy efficiency of water-splitting. The process involves four electrons' transfer and the generation of triplet state O₂ from singlet state species (OH⁻ or H₂O). Recently, explicit spin selection was described as a possible way to promote OER in alkaline conditions, but the specific spin-polarized kinetics remains unclear. Here, we report that by using ferromagnetic ordered catalysts as the spin polarizer for spin selection under a constant magnetic field, the OER can be enhanced. However, it does not apply to non-ferromagnetic catalysts. We found that the spin polarization occurs at the first electron transfer step in OER, where coherent spin exchange happens between the ferromagnetic catalyst and the adsorbed oxygen species with fast kinetics, under the principle of spin angular momentum conservation. In the next three electron transfer steps, as the adsorbed O species adopt fixed spin direction, the OER electrons need to follow the Hund rule and Pauling exclusion principle, thus to carry out spin polarization spontaneously and finally lead to the generation of triplet state O₂. Here, we showcase spin-polarized kinetics of oxygen evolution reaction, which gives references in the understanding and design of spin-dependent catalysts.

¹Beijing National Laboratory for Condensed Matter Physics and Institute of Physics, Chinese Academy of Science, Beijing, China. ²School of Material Science and Engineering, Nanyang Technological University, Singapore, Singapore. ³The Cambridge Centre for Advanced Research and Education in Singapore, 1 CREATE way, Singapore, Singapore. ⁴Key Laboratory of Advanced Material Processing & Mold (Zhengzhou University), Ministry of Education, Zhengzhou, China. ⁵MagnetoCat SL, Alicante, Spain. ⁶Energy Research Institute @ Nanyang Technological University, Singapore, Singapore. ✉email: htyang@iphy.ac.cn; xuzc@ntu.edu.sg

The sluggish kinetics of oxygen evolution reaction (OER) is a major cause for the low efficiency in techniques, such as solar water splitting,¹ rechargeable metal-air batteries,² regenerative fuel cells,³ and water electrolysis.^{4,5} Exploring better catalysts for OER has become increasingly attractive in recent years. Non-precious 3d-transition metal oxides (TMOs), such as Fe-, Co-, and Ni-based oxides, are promising cost-effective catalysts.^{6,7} Their catalytic activities are tunable as the diversity in oxides families affords numerous freedoms to tailor their physicochemical properties. Sabatier's principle, which qualitatively describes that the optimized catalytic activity when adsorbed species bind to the catalytic surface neither too strongly nor too weakly, led to the fundamental understanding of OER mechanisms and guided the subsequent design of highly active catalysts.^{8,9} This principle was further supported by the findings that the OER activities of transition metal oxides correlate strongly with the e_g occupancy, which is related to the binding strength between the metal and the oxygen species.^{10–12} Some exceptions have been found not well fitted with the e_g theory, which is partially resulted by the diverse and complicated magnetism in TMOs family.^{13–16} Besides, the produced O_2 is in triplet ground state, where the frontier π^* orbitals are occupied by two electrons with parallel alignment. In contrast, the ground spin state of reactant OH^-/H_2O is singlet with all paired electrons.^{17,18} The singlet states of the oxygen molecule were reported at an energy level of at least ~ 1 eV higher than its triplet state.^{18,19} Thus, the magnetism of TMOs, related to the spin polarization, should be influential on the kinetics of OER.^{20,21} It is reasonable to consider that the active sites with suitable thermodynamic paths for OER should allow a way to facilitate the spin alignment in the product. As suggested by recent theoretical studies by J. Gracia,^{22–24} the spin-polarized electrons in catalysts promote the generation of parallel spin aligned oxygen by quantum spin-exchange interactions (QSEI), which further promote the OER kinetics. Therefore, facilitating the spin polarization should be an effective strategy for improving OER efficiency. Ron Naaman and co-workers reported that the application of the chiral-induced spin selectivity effect to product the polarized electron. This spin polarization transferred is the origin of a more efficient oxidation process in which oxygen is formed in its triplet ground state.^{25–27} It has been pointed out by J. Gracia et al. that theoretically photosystem II can act as a spin-controlling gate to govern the charge and spin transport during the OER process,²⁸ which offers a favoured thermodynamic path for O_2 evolution. Besides the extrinsic spin polarizer, the ordered magnetic moment structure in ferromagnetic materials can create intrinsic spin filtering for highly spin-polarized electrons. The spin filtering effect originates from the exchange splitting of the energy levels in the conduction band of a magnetic insulator.²⁹ Most recently, José Ramón Galán-Mascarós et al. reported an external magnetic field, applied by a permanent magnet, enhances the OER activity of magnetic oxides in alkaline.³⁰ It opens a new strategy to manipulate the spin polarization in magnetic oxide catalysts for promoting the OER and encourages more detailed studies to understand how the magnetic field induced spin polarization affects the OER process.

In this work, we report an investigation on the key kinetics change on the ferromagnetic $CoFe_2O_4$ catalyst under the magnetic field. The ferromagnetic $CoFe_2O_4$ catalyst works as a spin polarizer under the magnetic field. We have found that the spin-polarized kinetics of OER starts at the first electron transfer step, where ferromagnetic exchange happens between the ferromagnetic catalysts and the adsorbed oxygen species (reactants) under the principle of spin angular momentum conservation. Without the magnetic field, the Tafel slope of $CoFe_2O_4$ is identical and equal to circa 120 mV/decade, which indicates the

first electron transfer step is rate-determining step (RDS) and no electron transfer occurring before the RDS. Under the magnetic field, the Tafel slope decreases to circa 90 mV/decade, indicating the number of electron transfer is ~ 0.5 and a mixed RDS involving the first electron transfer step and second steps. Such a phenomenon cannot be observed in the catalysts without ferromagnetic orderings under the same condition. The results indicate that the key step of spin-polarized OER is the first electron transfer step in OER, where the spin-polarized process via exchange hopping can be facilitated under the magnetic field. As a consequence, the first electron transfer is no longer the RDS. After a facilitated spin-polarized ferromagnetic exchange of electrons, the adsorbed O species will overall settle on the fixed spin direction. Due to the Hund Rule and Pauli Exclusion Principle, the follow-up electrons' transfer needs to carry out spin polarization spontaneously and finally lead to the generation of triplet state oxygen. Overall, we showcase the key kinetics information in OER under a magnetic field, which influences the micro- and macroscopic spin polarization and spin transport. This finding will be helpful for further development of magnetic field assisted OER-enhancing strategy and related catalysts.

Results

Magnetic and electrochemical characterizations. We begin with the discussion of the magnetic properties of the employed catalysts, $CoFe_2O_4$, Co_3O_4 , and IrO_2 . The study will determine the suitable magnetic field and whether a global aligned magnetic moment can be achieved. The study of magnetic property reveals the optimal strength of the applied magnetic field for the alignment of the magnetic moment in ferromagnetic $CoFe_2O_4$. The $CoFe_2O_4$ and Co_3O_4 were prepared by a modified solid-state chemistry method as previously reported.¹¹ X-ray powder diffraction characterization was performed to confirm their crystal structures. The diffraction patterns match well with the standard patterns without impurity peak found (Supplementary Fig. 1 and Supplementary Table 1). As depicted in Fig. 1a, $CoFe_2O_4$ gives a hysteresis loop in an enlarged manner, indicating a room-temperature ferromagnetic behavior with a saturation magnetization (Ms) of $44 \text{ emu}\cdot\text{g}^{-1}$. The Co_3O_4 and IrO_2 samples with tiny susceptibility (χ) of 3.07×10^{-5} and 0.51×10^{-6} , respectively, at 300 K show antiferromagnetic or paramagnetic behaviors, respectively. The detailed magnetic data are summarized in Supplementary Table 1. The cyclic voltammetry (CV) of those catalysts were then measured with and without a constant magnetic field of 10,000 Oe under alkaline condition (see Methods for details). As shown in Fig. 1b, c, d, the OER performance of the ferromagnetic $CoFe_2O_4$ is promoted obviously under the magnetic field while the changes in non-ferromagnetic catalysts Co_3O_4 and IrO_2 are negligible. When a strong enough magnetic field (higher than the coercivity) is applied to a ferromagnetic material, the magnetic moment will (macroscopically) align along with the direction of the external magnetic field. The ferromagnetic (long-) ordered material as spin polarizer is an extended selective spin-filter for electron transfer during catalysis. The generation process of polarized electrons has been illustrated in Fig. 1e.

It should be noticed that the use of magnetic fields in water electrolysis has been studied in the past,^{31–36} in which the mass transport in the electrochemical process was found to be affected by the Lorentzian movement, i.e. the diffusion of reagents and the release of the generated gas bubbles are promoted. However, in this study, some evidence has excluded such effect from mass transport as a main contributor to OER enhancement under the magnetic field. First, the improvement was not observed on

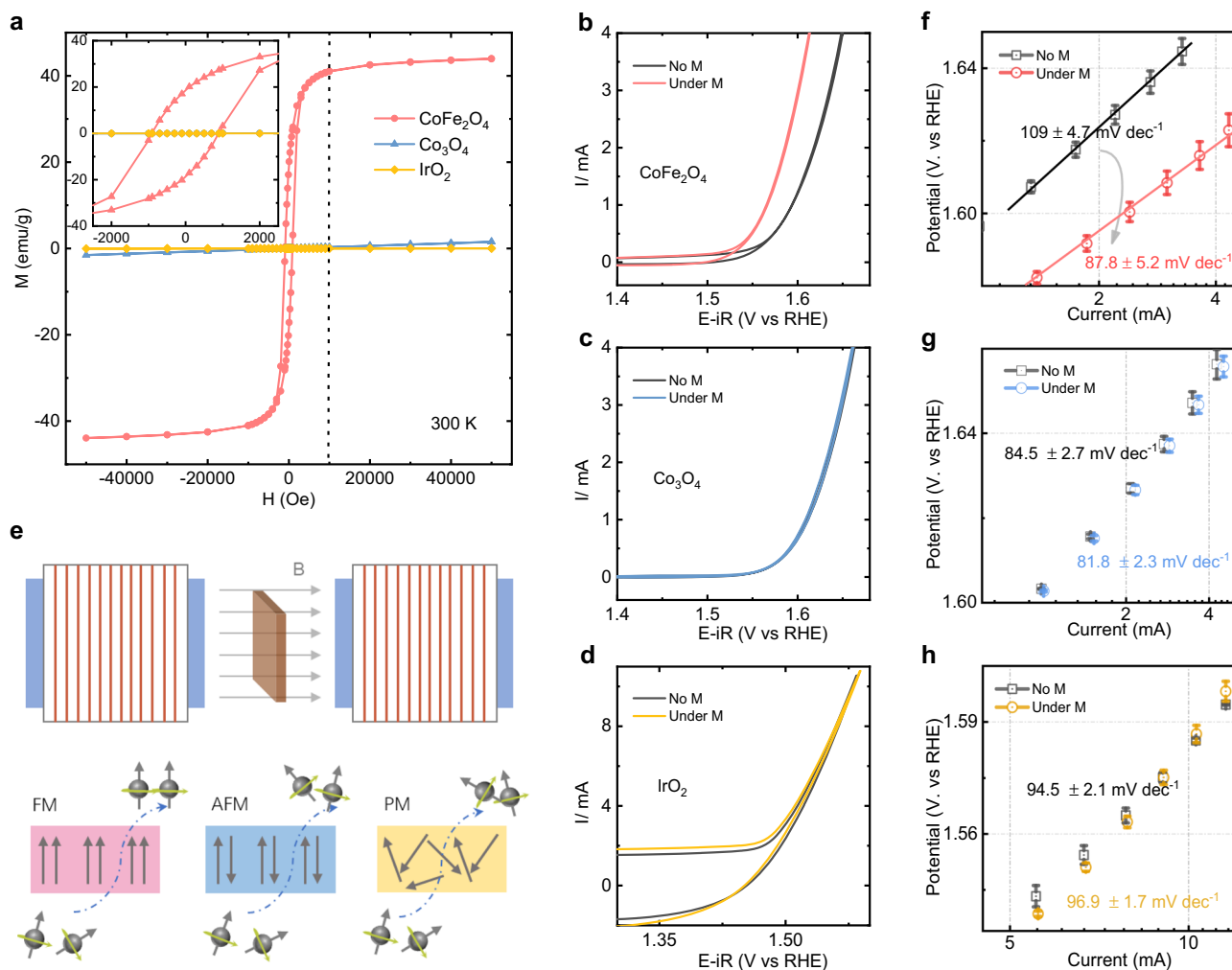


Fig. 1 Spin polarization promotes OER. **a** Magnetic hysteresis loops of CoFe_2O_4 , Co_3O_4 , and IrO_2 powders at room temperature (300 K) and the magnified graph inset in the top left of this panel. (Here, IrO_2 powder is a commercial catalyst (bulk, Premetek). Cyclic voltammetry (CV) of CoFe_2O_4 (**b**), Co_3O_4 (**c**), and IrO_2 (**d**) catalysts at a scan rate of 10 mV/s in O_2 -saturated 1M KOH with and without a constant magnetic field (10,000 Oe). **e** The schematic of the generation of the polarized electron under a constant magnetic field. The Tafel plots of CoFe_2O_4 , (**f**) Co_3O_4 (**g**), and IrO_2 (**h**) catalysts with and without a constant magnetic field (10,000 Oe). The error bar represents three independent tests.

non-ferromagnetic catalysts Co_3O_4 and IrO_2 with the effect of Lorentzian movement on mass transport. Second, we also tested the OER performance of $\text{Co}(\text{acac})_2$ and $\text{Fe}(\text{acac})_3$ with and without a constant magnetic field (as shown in Supplementary Fig. 2). Nearly no difference can be observed. It also should be noted that OH^- and H_3O^+ in aqueous solution do not move physically, but by sequential proton transfer, known as Grotthuss mechanisms³⁷ (Supplementary Fig. 3). That means the influence of Lorentz force on the physical movement of ions OH^- or H_3O^+ is negligible. Thus, the effect from the mass transport under the external magnetic field should have little contribution to the observed OER enhancement of the ferromagnetic CoFe_2O_4 . Besides, the electrical resistance of magnetic materials can be affected by the magnetization, which is through the scattering of electrons on the magnetic lattice of the crystal.^{38–40} However, the difference in the conductivity at room temperature under 10,000 Oe is about 3% for insulator CoFe_2O_4 with 3.86×10^{-5} S/m,^{40–42} which does not cause a significant difference in the electrode's conductivity. This is because acetylene black carbon (AB) with 500 S/m as a conductive mediator is mixed with those oxide catalysts for their application as the electrode,⁴³ which dominates the electron conduction.

No surface restructuring in OER. It is generally recognized that some Co-based perovskites and spinels undergo operando surface reconstruction to form active Co (oxy) hydroxides in alkaline conditions to promote OER.^{44–46} In our case, there are no changes in OER performance of CoFe_2O_4 during CA tests in 1M KOH for 1 h shown in Supplementary Fig. 4, indicating CoFe_2O_4 is stable without noticed surface reconstruction during the OER process. The high-resolution transmission electron microscope (HRTEM) was further used to rule out the possible interference from surface reconstruction of catalysts during the OER. It has been found that the spinel crystal structure of CoFe_2O_4 remained after the electrochemical treatment (Supplementary Fig. 5), which is consistent with what has been reported previously.⁴⁷ The aberration-corrected STEM provides direct atomic imaging and confirms that the well-crystalline feature reserved from the surface to bulk (Fig. 2a, b). The HADDF line profile shows the same bond length of Co-O in bulk and surface, which verifies no surface reconstruction (Fig. 2c). Raman technique was then performed to study the inhomogeneity evolution in the near-surface region. The Raman spectra of cubic structures (Fd-3m) CoFe_2O_4 before and after OER are presented in Fig. 2d. In the top curve, peak maxima at 603 and 666 cm^{-1} are due to

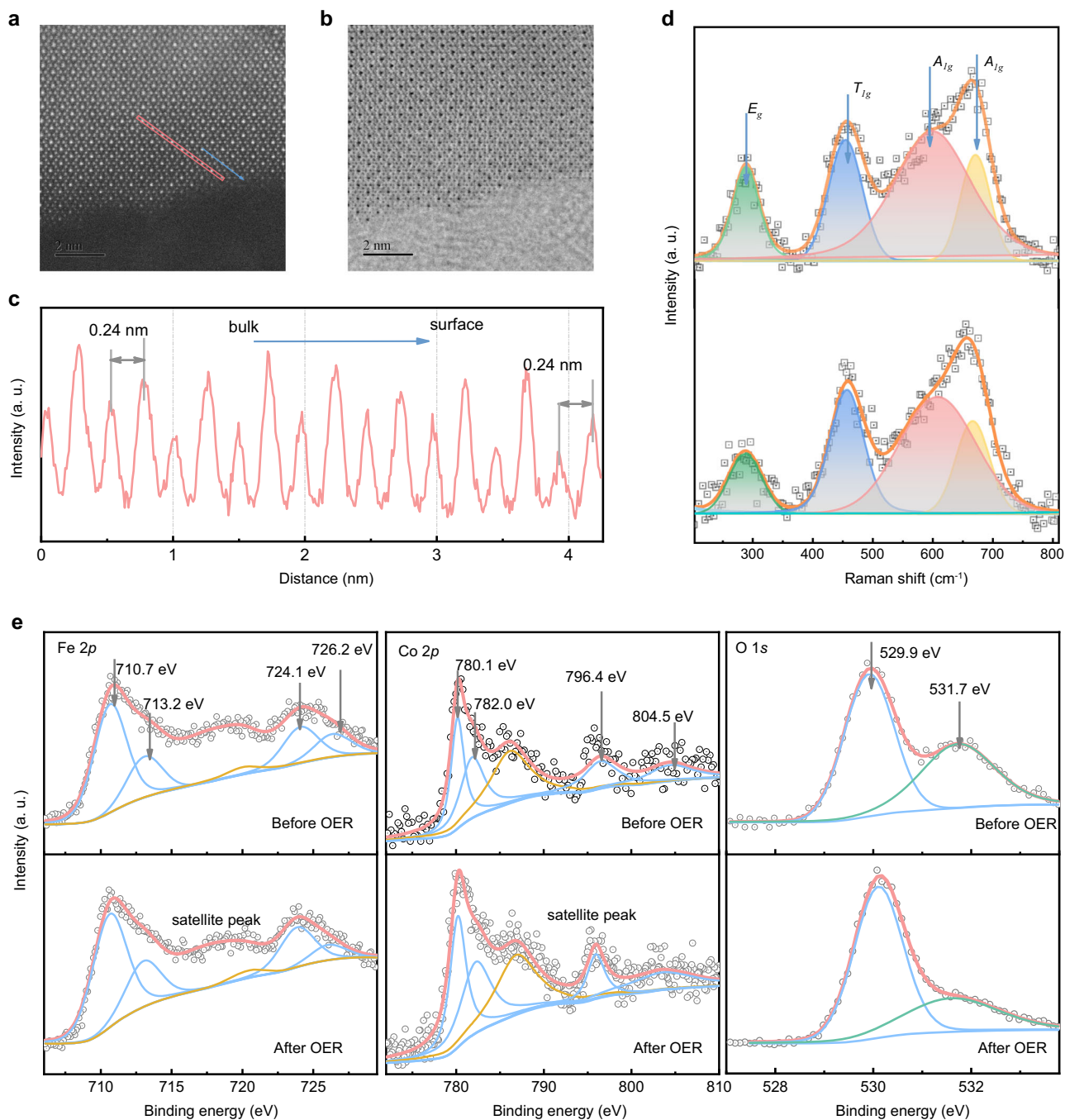


Fig. 2 No surface restructuring on CoFe_2O_4 . HADDF (a) and ABF (b) images of CoFe_2O_4 after OER. The line profiles of HADDF (c) acquired at the pink line rectangular zone. d Raman spectra of CoFe_2O_4 before and after OER. e The Fe 2p, Co 2p, and O 1s XPS spectra results of CoFe_2O_4 before and after OER.

A_{1g} symmetry involving symmetric stretching of oxygen atom with respect to the metal ions in tetrahedral sites. The other low-frequency phonon modes are due to metal ions involved in octahedral sites, i.e. E_g and T_{1g} . The assignment of these phonon modes was carried out in accordance with the literature.⁴⁸ After electrochemical treatment (bottom curve), no changes in the vibrational modes were observed, which proves once again that there is no surface reconstruction in OER. X-ray photoelectron spectroscopy (XPS) was also performed to study the surface chemical states of CoFe_2O_4 before and after the OER. As shown in Supplementary Fig. 6, the XPS survey spectra confirm the coexistence of Co, Fe, and O in the samples. Figure 2e shows

the 2p orbital of Fe, Co, and 1s orbital of O. The XPS of Fe 2p core level presents two pairs of peaks: $\text{Fe}^{3+} 2p_{3/2}$ at about 710.7 eV and 713.2 eV; $\text{Fe}^{3+} 2p_{1/2}$ at about 724.1 eV and 726.2 eV. The doublets in samples can be ascribed to Fe^{3+} in octahedral sites and Fe^{3+} in tetrahedral sites, respectively. The two peaks of Co 2p with the binding energy of 780.1 and 782.0 eV are ascribed to Co^{2+} ions in octahedral sites and Co^{2+} ions in tetrahedral sites. The main peaks of O 1s at 529.6 eV are recognized as oxygen ions, which are all associated with a “−2” formal charge.⁴⁹ Compared to the spectra before and after the OER, these peaks remain unchanged in location, indicating no surface reconstruction.

Spin-polarized kinetics of OER. Oxygen evolution reaction is authenticated a four-step reaction with each step accompanied by an electron transfer. The Tafel plots are widely regarded as a generalized kinetics theory for electron transfer reactions. The Tafel equation presents the relationship between the Tafel slope and the exchange current density:

$$\eta = -\frac{2.303 RT}{\alpha F} \times \log i_0 + \frac{2.303 RT}{(\alpha + n)F} \times \log i \quad (1)$$

where the Tafel slope equals to $2.303RT/[(\alpha + n)F]$ (i_0 is the exchange current density, R is the universal gas constant, T is the absolute temperature, F is the Faraday constant, n is the number of electrons transferred before RDS, and α is the charge transfer coefficient and usually assumed to be 0.5).^{50,51} Ideally, the Tafel slope tells the information of reaction kinetics. For example, the Tafel slope is $120 \text{ mV}\cdot\text{dec}^{-1}$, which indicates the first electron transfer step is the RDS because there is no electron transfer before the RDS. If the second step is the RDS, the Tafel slope will decrease to $40 \text{ mV}\cdot\text{dec}^{-1}$ with an electron transfer number of 1. The change of the Tafel slope is often reputed as an indication of the change of reaction mechanism. As shown in Fig. 1f, the Tafel slope of CoFe_2O_4 is about $109 \pm 4.7 \text{ mV}\cdot\text{dec}^{-1}$ and that indicates the first electron transfer from the adsorbed OH^- is the RDS without the magnetic field. But, after applying a constant magnetic field, the Tafel slope decreases to circa $87.8 \pm 5.2 \text{ mV}\cdot\text{dec}^{-1}$, indicating the number of electron transfer is about 0.5 and a mixed RDS involving the first electron transfer step and second steps. Furthermore, we have carried out OER measurements of CoFe_2O_4 , Co_3O_4 , and IrO_2 under different temperatures as shown in Fig. 3a. We first noted that the OER performance of catalysts is getting better as the reaction temperature increases. This is probably because that the rate constant of the reaction will increase as the reaction temperature increases, which can promote this reaction based on the transition state theory⁵². More importantly, the OER performance of the ferromagnetic CoFe_2O_4 is promoted under the magnetic field at various temperature. However, the positive influence of the magnetic field on the OER performance of CoFe_2O_4 is decreased as the reaction temperature increases. The corresponding Tafel slopes are shown in Fig. 3b. At room temperature, the Tafel slope of CoFe_2O_4 is about $106 \text{ mV}\cdot\text{dec}^{-1}$ without the magnetic field. After applying a constant field, the Tafel slope decreases to circa $82.8 \text{ mV}\cdot\text{dec}^{-1}$. As the temperature increases, the positive influence of the magnetic field became not that remarkable. This is because the arrangement of magnetic moments of catalyst will be thermally disturbed. The ferromagnetic ordering in the catalyst gets disturbed and thus a certain degree of demagnetization at high temperature occurs, which lead to the decreased influence of the magnetic field on OER. We also note that the Tafel slopes of CoFe_2O_4 have a slight favorable change as temperature increases, which maybe because the interaction between two M-O unites mechanism occurs at high temperature.^{53,54} Thus, the key step in spin-polarized OER is the first electron transfer step in FM CoFe_2O_4 , where the adsorbed OH^- is difficult to deprotonate and transfer the electron. However, the change of Tafel slopes was not observed in the non-ferromagnetic catalysts under the same condition.

The electron transfer at the catalytic interface depends on the transition probability, which is associated with the wavefunction integral between OH^- and the active site. As revealed by our previous work, the octahedral sites are mainly responsible to the OER⁵⁵. The extended X-ray absorption fine structure (EXAFS) showed the perfect inverse spinel structure of CoFe_2O_4 (Supplementary Fig. 7). The Fe^{3+} ions distribute equally in octahedral and tetrahedral sites and Co^{2+} ions distribute in octahedral sites. We further calculated the effective magnetic moment (μ_{eff}) of

CoFe_2O_4 to be about $3.44 \mu_{\text{B}}$ by Curie–Weiss fitting (Supplementary Fig. 8). The μ_{eff} for CoFe_2O_4 is very close to the idea value of the inverse spinel.⁵⁶ Thus, the Co^{2+} ions in octahedral sites contribute to the effective ferromagnetic moment. Those results are consistent in previous experimental work.⁵⁷ Considering that only Co in octahedral sites contribute the effective magnetic moment, the magnetic field enhanced OER should mainly happen on the Co sites. Thus, we studied the Co sites as the active sites in this work. For a ferromagnetic (FM) catalyst, the orbitals of the FM oxides create an intrinsically degenerate spin-polarized metallic state that optimizes the wavefunction based on the inter-atomic reduction of the electron–electron repulsion. DFT calculations were performed to explore the different electron structure of CoFe_2O_4 under an applied magnetic field (The computational details are shown in the Supplementary Information). As shown in the projected density of states (PDOS) of CoFe_2O_4 (Fig. 4a), there is more overlap between the line of M-3d and the line of O-2p after spin alignment, which indicates the 3d-2p hybridization of the CoFe_2O_4 become stronger⁵⁸ after spins are aligned. As well, compared to the CoFe_2O_4 with anti-parallel couplings, the CoFe_2O_4 with spin alignment has a higher spin density on the oxygen atoms (Fig. 4b). The calculation indicates that the magnetic moment of the ligand hole in CoFe_2O_4 is $0.059 \mu_{\text{B}}$ without spin alignment and is $0.188 \mu_{\text{B}}$ with spin alignment, which indicates a FM ligand hole in CoFe_2O_4 . A concomitant increment of the 3d-2p hybridization associate with FM ligand holes will facilitate spin-selected charge transport and optimize the kinetics of the spin-charge transfer in the three-phase interface.^{43,59} Thus, the dominant FM exchange between the ferromagnetic catalyst and the adsorbed oxygen species (reactants) will happen (Fig. 4c and Supplementary Figure 9) with smaller electron–electron repulsion, which induce spin-dependent conductivity and decrease the rate-limiting bonding energies, making that the first electron transfer is no longer the RDS. We further prepared the Pourbaix diagram of CoFe_2O_4 as shown in Fig. 4d, which show that the surface termination of CoFe_2O_4 is oxygen termination under OER conditions. The reaction started between a ligand oxygen on the surface and the adsorbed oxygen species (OH^-), and the “first” electron transfer step is $\text{O}^* + \text{OH}^- \rightarrow \text{*OOH} + \text{e}^-$. The spin-related OER mechanisms show in Fig. 4e. The FM CoFe_2O_4 with FM ligand hole will form oxygen termination with fixed spin direction. The first electron transfer process led to the generation of $\text{O}(\downarrow)^-$, that is, the first electron transfer step is spin-polarization process to form the triplet state intermediate $\text{O}(\downarrow)\text{O}(\downarrow)\text{H}$ species with a lower barrier (Supplementary Fig. 10). Consequently, the triplet state intermediate $\text{O}(\downarrow)\text{O}(\downarrow)\text{H}$ species will prefer to generate the triplet state O_2 . We also conducted a DFT study on the free energies of OER steps on the (111) surface of CoFe_2O_4 with and without spin alignment. Please be noted that here the topmost layer of the slab model is fully relaxed in the calculations since there is little difference between the one-layer-relaxed model and the two-layer-relaxed model, which can be also found in literature⁶⁰. The calculation model of CoFe_2O_4 is shown in Supplementary Fig. 14. The (111) surface is chosen because the TEM investigation found the surface is rich in (111) and there is no remarkable change on the surface after OER (Supplementary Fig. 11). The energy diagram for these two paths at 1.23 V (vs RHE)^{61,62} to produce triplet oxygen is shown in Fig. 4f. The active sites with spin alignment are more thermodynamically favourable to OER, if they associate with ferromagnetic ligand holes,⁵⁹ and the overpotential of producing triplet oxygen is reduced by 390 mV compared to that without aligning spin. The coordinated inter-atomic aligned spin on active sites plays an important role in optimizing the spin-dependent reaction coordinates.

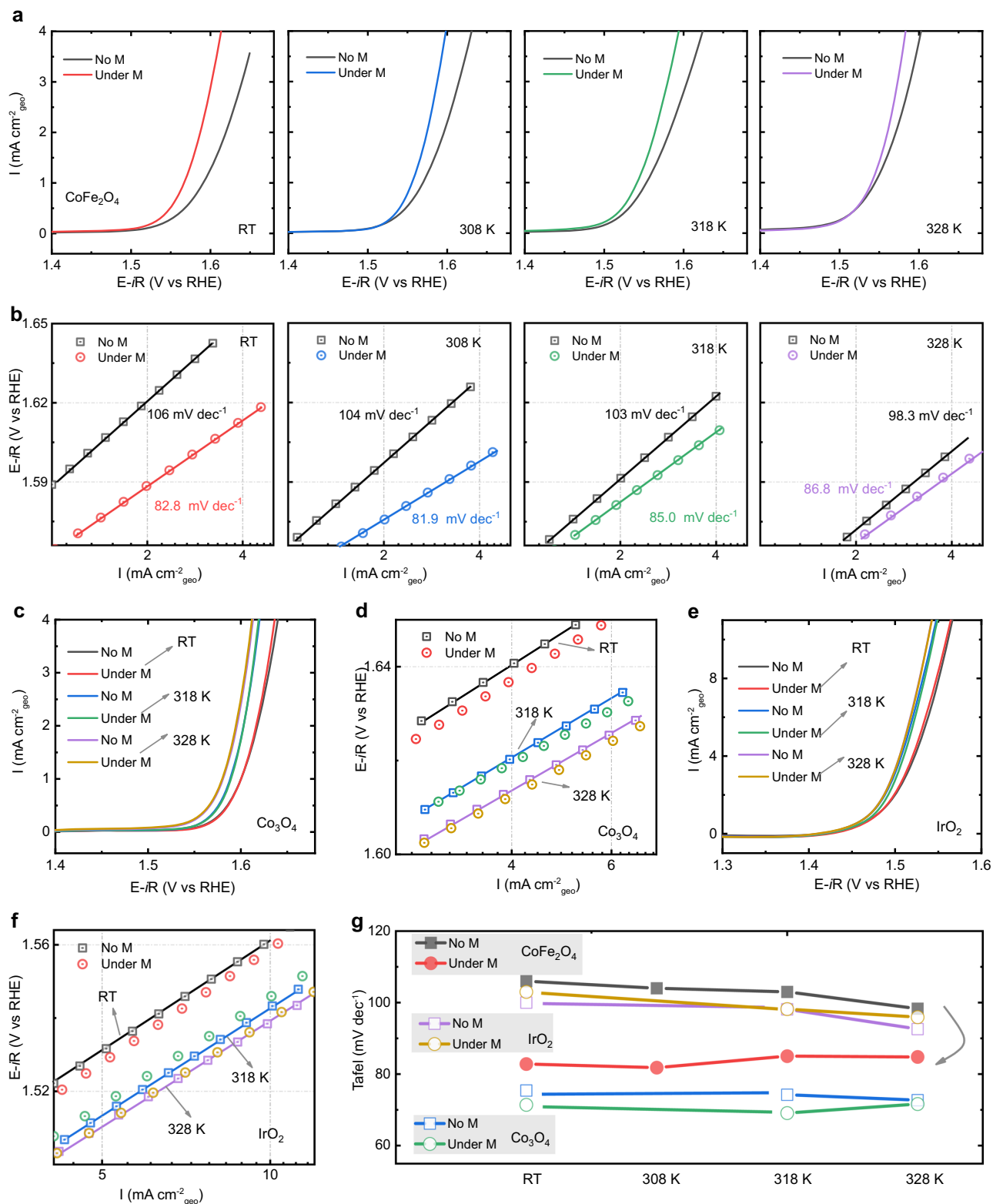


Fig. 3 OER under the different temperature. **a** LSV curves of CoFe_2O_4 at a scan rate of 10 mV/s in O_2 -saturated 1 M KOH with and without a constant magnetic field (10,000 Oe) under the different temperatures (room temperature (RT): \sim 303 K, 308 K, 318 K, and 328 K). The corresponding Tafel plots are shown in **b**. **c** LSV curves of Co_3O_4 with and without a constant magnetic field (10,000 Oe) under the different temperatures (room temperature (RT): \sim 303 K, 313 K, and 323 K). The corresponding Tafel plots are shown in **d**. **e** LSV curves of IrO_2 with and without a constant magnetic field (10,000 Oe) under the different temperatures (room temperature (RT): \sim 303 K, 313 K, and 323 K). The corresponding Tafel plots are shown in **f**. Tafel slopes at various temperatures are summarized in **g**.

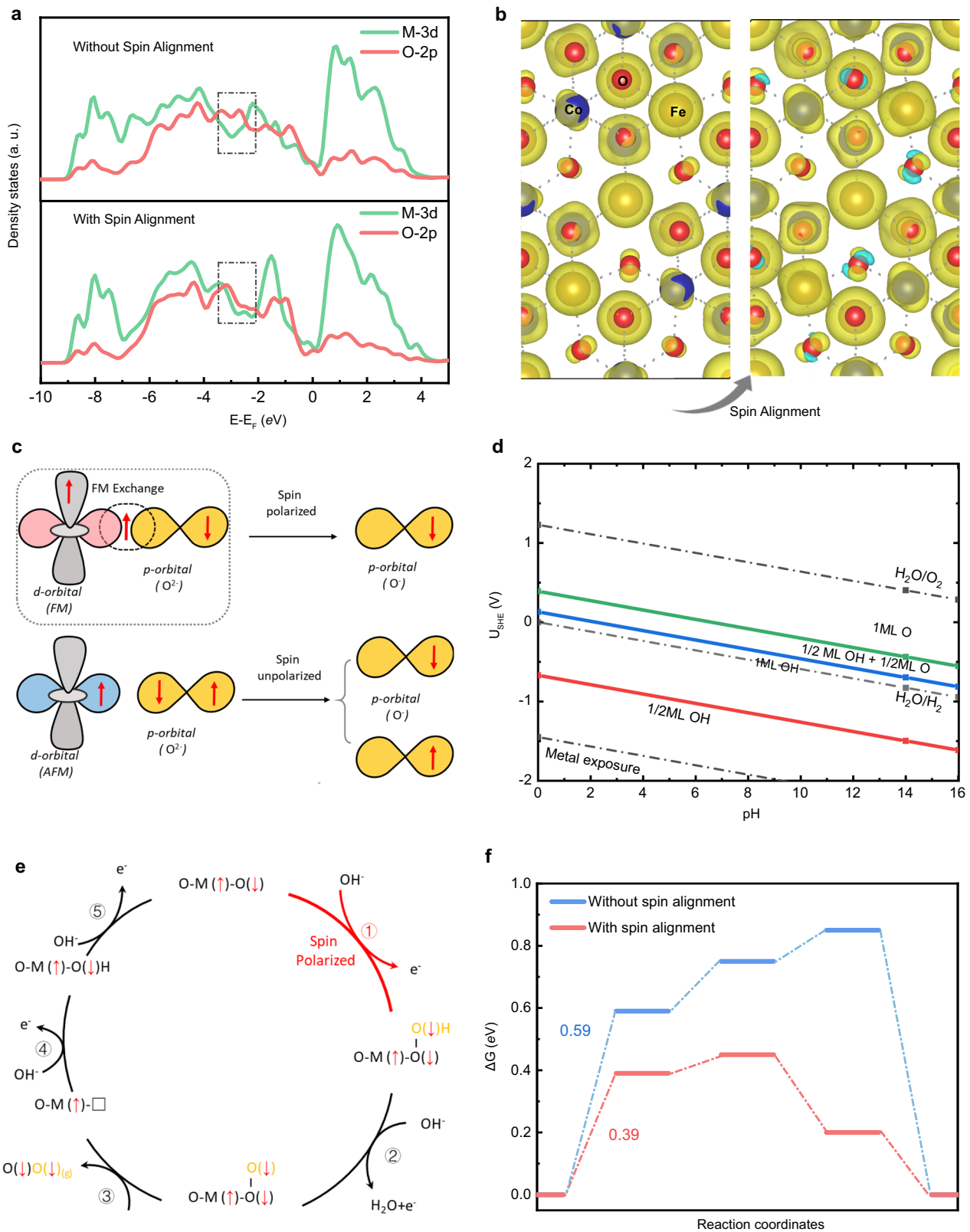


Fig. 4 Spin-polarized OER. **a** The projected density of states (PDOS) of CoFe_2O_4 without and with spin alignment. **b** The spin density for CoFe_2O_4 with and without spin alignment. **c** Schematic of spin-exchange mechanism for OER. The first electron transfer step is promoted by spin polarization through the FM exchange (QSEI), which gives smaller electronic repulsions and makes the adsorbed O species have a fixed spin direction. **d** The calculated Pourbaix diagram of the (111) surface of CoFe_2O_4 . **e** The spin-polarization mechanisms in OER with starting from the step of $\text{O}^* + \text{OH}^- \rightarrow ^*\text{OOH} + \text{e}^-$ step. **f** The free energy diagram of OER at 1.23 V (vs. RHE)^{61,62} with and without the spin alignment on the (111) surface of CoFe_2O_4 toward triplet oxygen production.

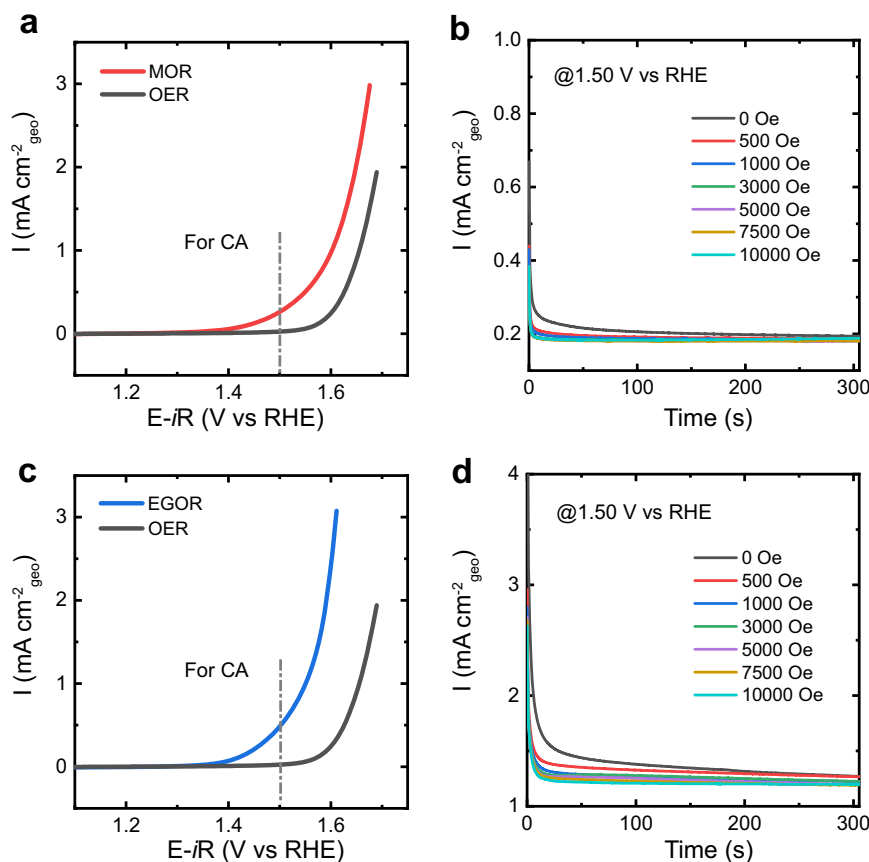


Fig. 5 No influence on MOR and EGOR. **a** Linear sweep voltammetry (LSV) curves of MOR at a scan rate of 10 mV/s in 1 M KOH in the presence of 1 ml methanol. **b** Chronoamperometry (CA) experiments of MOR were performed at a constant potential of 1.50 V (versus RHE). **c** LSV curves of EGOR at a scan rate of 10 mV/s in 1 M KOH in the presence of 1 ml ethylene glycol. **d** The CA curves of EGOR at 1.50 V vs. RHE.

It is worth noting that OER requires the generation of paramagnetic O_2 molecules starting from diamagnetic species (OH^- and H_2O). For a reaction involving non-magnetic molecules only, not impact significantly on the reaction kinetics. We investigated the methanol oxidation reaction (MOR) and ethylene glycol oxidation reaction (EGOR) on $CoFe_2O_4$ under the magnetic field. Here, changes in FM catalyst conductivity caused by magnetic fields can be ignored because that AB mediator is also mixed with $CoFe_2O_4$ for their application as the electrode, which dominant the electron conduction. Figure 5 reveals that there is no remarkable difference in these reactions under the magnetic field. This is because the reactants, intermediates, and the products in these reactions are diamagnetic and there is no spin-selected electron transfer between the active metal site and the adsorbed reaction species.

The effect of gradient magnetic field, remanence, and demagnetization. It is known that for ferromagnetic materials, the magnetic moment pertains to the spin. The more ordered its magnetic moment is, the higher the degree of positive spin polarization is. As observed in the initial magnetization curve of $CoFe_2O_4$ (Fig. 6a), its magnetic moments become more orderly as the magnetic field increases, before reaching the saturation field. We then investigated the effect of the gradient magnetic field on OER activity. We carried out a series of CA measurements under the different magnetic field strength at a constant potential of 1.66, 1.66, and 1.56 V (versus RHE) for $CoFe_2O_4$, Co_3O_4 , and IrO_2 , respectively (Fig. 6b). It can be seen that the current density of the ferromagnetic catalyst $CoFe_2O_4$ increases with the increase of the magnetic field strength. For non-ferromagnetic Co_3O_4 and

IrO_2 , there is almost no change when changing the field strength. The increment of the current density is summarized in Fig. 6c. The increase of spatial spin polarization related to the degree of magnetization shows a positive correlation with the enhancement of the OER for ferromagnetic $CoFe_2O_4$. We also measured the LSV curves of all oxides before and after the CA experiment. As seen in Supplementary Fig. 12, the OER performance ferromagnetic $CoFe_2O_4$ can be further improved after the CA test under magnetic field, but not for non-ferromagnetic Co_3O_4 and IrO_2 . An interesting finding is that the OER performance of $CoFe_2O_4$ remains even after the magnetic field is removed (Fig. 6d). This is because the magnetic moment is still aligned in magnetized $CoFe_2O_4$ (Fig. 6e) after removing the magnetic field, which persists as the spin polarizer to create spin polarization. This is an important fact to make clear that the enhancement is due to the indirect (strong) QSEI, and not due to weak direct spin-spin interactions from the external field, a typically conceptual error. More interestingly, when the magnetized $CoFe_2O_4$ was demagnetized using an oscillating magnetic field (Fig. 6g), the OER performance of $CoFe_2O_4$ reverted to the initial value before the field was applied. The Tafel slope of $CoFe_2O_4$ is back to 120 mV dec^{-1} , indicating the first electron transfer of the adsorbed OH^- is again the RDS, same as the status without the magnetic field. Based on the above results, we can confirm that the spin polarization facilitated OER is reversible and adjustable.

Discussion

It is found that ferromagnetic $CoFe_2O_4$ serves as the spin polarizer facilitates the spin polarization under a constant magnetic field. The increase of spatial spin polarization shows a positive

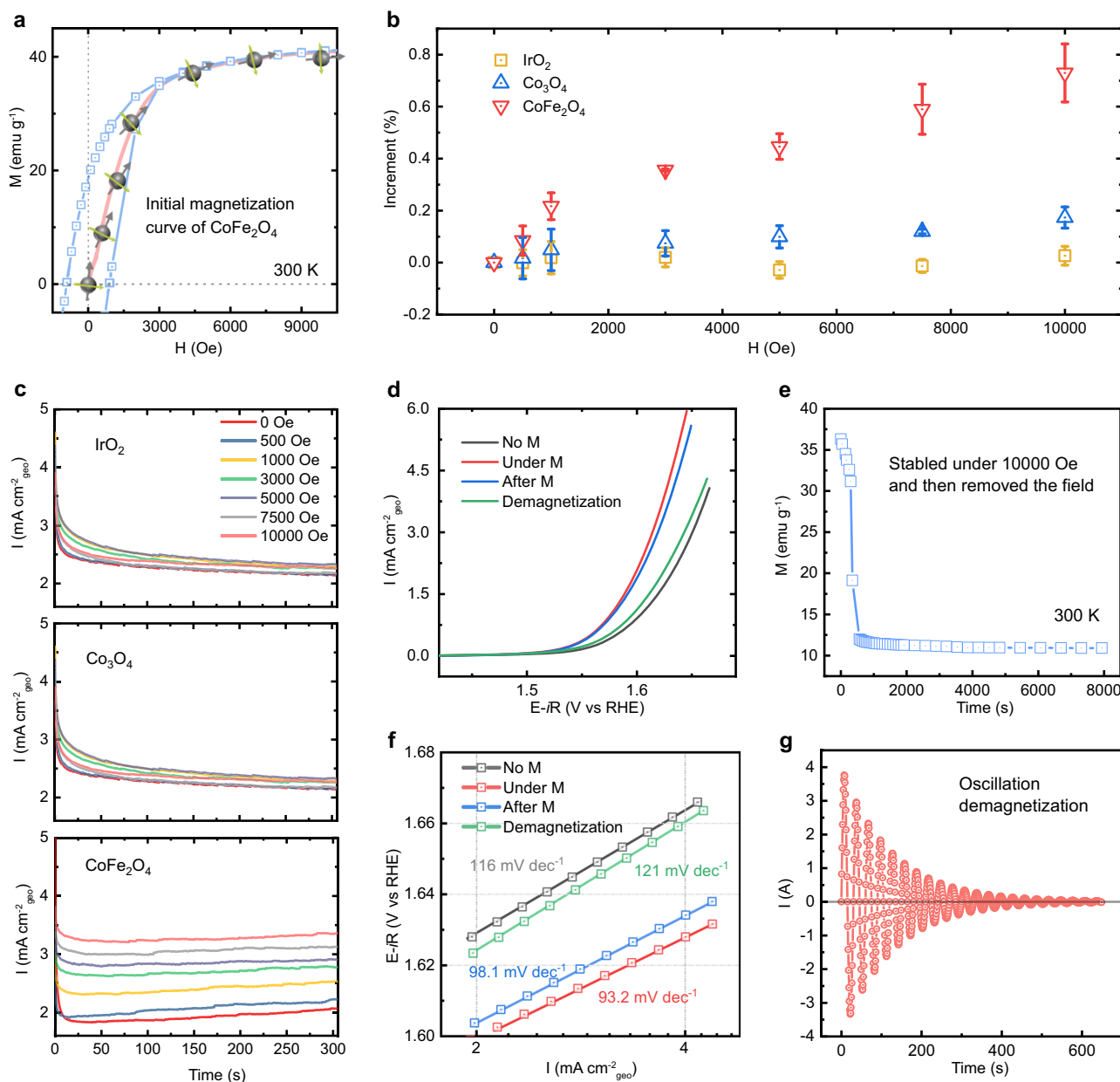


Fig. 6 The effect of gradient magnetic field, remanence, and demagnetization. **a** Initial magnetization curve of CoFe_2O_4 . **b** CA test in 1M KOH under the different magnetic field strength (0, 500, 1000, 3000, 5000, 7500, and 10000 Oe) at a constant potential of 1.66 V versus RHE for CoFe_2O_4 , Co_3O_4 , and 1.56 V versus RHE for IrO_2 . **c** The increment of the current density under different magnetic field strength. It was calculated by the following equation: $\text{Increment (\%)} = (j_M - j_{M=0})/j_{M=0}$; j_M is the chronopotentiometry current density values obtained under the applied magnetic fields (0, 500, 1000, 3000, 5000, 7500, and 10000 Oe). The error bar represents three independent tests. **d** LSV curves of CoFe_2O_4 at a scan rate of 10 mV/s in O_2 -saturated 1M KOH with and without a constant magnetic field (10,000 Oe), after the magnetic field removed (after M), and after demagnetization. The corresponding Tafel plots are shown in **f**. **e** The magnetization of CoFe_2O_4 after removing a constant magnetic field of 10,000 Oe. **g** The curve of demagnetization for CoFe_2O_4 .

correlation with the enhancement of spin transport (selection) during OER. We have found that the Tafel slope of overall ferromagnetic CoFe_2O_4 switched from ~ 120 to $\sim 90 \text{ mV} \cdot \text{dec}^{-1}$ after applying a magnetic field. It indicates the change of the RDS of OER reaction under an external magnetic field, i.e. the first electron transfer step is no longer the RDS. The spin-polarized electron exchange between the ferromagnetic CoFe_2O_4 and the adsorbed oxygen species (reactants) for the first electron transfer is ferromagnetic-exchange-like under the principle of spin angular momentum conservation, which leads to faster reaction kinetics

for the first electron transfer step. In contrast, such a phenomenon was not observed on non-ferromagnetic catalysts. The findings imply that the conservation of the total spin on the active sites during OER is an important concept, which applies quantum spin-exchange interactions to optimize reaction kinetics. The kinetic improvement maintains after the removal of the external magnetic field. The demagnetization can bring the activity back to that before magnetization. This work provides new understandings of the effect of an external magnetic field on the OER activity of a ferromagnetic catalyst.

Methods

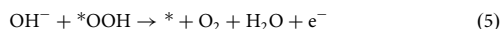
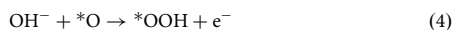
Material synthesis. Spinel CoFe_2O_4 oxides were synthesized by a modified conventional solid-state chemistry method as described elsewhere⁴⁵ with $\text{Fe}(\text{NO}_3)_2$ and $\text{Co}(\text{NO}_3)_2$ as precursors. 9 mmol mixture of $\text{Fe}(\text{NO}_3)_3 \cdot 9\text{H}_2\text{O}$ (Alfa Aesar) and $\text{Co}(\text{NO}_3)_2 \cdot 6\text{H}_2\text{O}$ (Sigma-Aldrich) was dissolved in 15 mL of DI water, followed by stirring and vaporizing in oven at 80 °C. The resulting slurry was calcinated at 250 °C for 2 h in the air to decompose nitrous completely. After grinding, the black oxide powders underwent calcination in air at 400 °C for 8 h. Co_3O_4 oxides were synthesized by the same method.

Electrochemical characterizations. The OER tests were operated in a three-electrode cell with a working electrode (WE) of glassy carbon flake ($10 \times 20 \times 0.5$ mm; Effective electrode area: 1.0 cm^2), a counter electrode of platinum foil, and a Hg/HgO reference electrode (RE) (filled with 1 M KOH solution). The catalysts electrode was fabricated by the recipe drop-castes method, which was reported in elsewhere⁶³. The catalysts were mixed with acetylene black (AB) at a mass ration of 5:1, then were dispersed in isopropanol/water (v/v = 1:4) solvent followed by the addition of Na^+ -exchanged Nafion as the binder. The mixtures were ultrasonicated for 30 min to reach homogeneous ink. The concentration of oxides in ink is 5 mg/ml, and AB is 1 mg/ml. Before drop-casting, the glassy carbon electrodes were polished to a mirror finish with $\alpha\text{-Al}_2\text{O}_3$ (50 nm) and washed by IPA and water to clean up completely. Finally, the as-prepared ink (100 μl) was dropped onto glassy carbon electrodes to reach a loading mass of 500 $\mu\text{g}_{\text{ox}} \text{ cm}^{-2}$ and the electrodes were dried overnight at room temperature. Cyclic voltammograms (CVs), linear sweep voltammetry (LSV), and chronoamperometry (CA) were performed in O_2 -saturated 1 M KOH by using Bio-logic SP 150 potentiostat. All potentials were converted to RHE scale according to the following equation: $\text{RHE} = \text{Hg/HgO} + 0.098$ with iR correction. The tests of methanol oxidation reaction (MOR) and ethylene glycol oxidation reaction (EGOR) on CFO electrodes are similar to the OER test. The difference is that the MOR and EGOR were studied in 1 M KOH 100 ml electrolyte in the presence of 1 ml methanol and 1 ml ethylene glycol, respectively⁶⁴.

Materials characterizations. The X-ray diffraction (XRD) of oxides were carried on Bruker D8 diffractometer at a scanning rate of 2° min^{-1} , under $\text{Cu-K}\alpha$ radiation ($\lambda = 1.5418 \text{ \AA}$). DC magnetization measurements were performed on a Superconducting Quantum Design (SQUID) magnetometer (MPMS-XL). The SQUID measurements of the magnetization of samples as a function of the magnetic field were carried out at 300 K in fields between -5 T and $+5 \text{ T}$. The high-resolution transmission electron microscopy (HRTEM) was carried JEOL JEM- 2100 plus microscope at 200kV. The STEM results presented here were obtained using the 200 kV JEOL ARM electron microscope equipped (JEOL, Tokyo, Japan) with double aberration correctors, a dual-energy-loss spectrometer and a cold field emission source. The atomic-resolved STEM images were collected with a condense aperture of 28 mrad and a collection angle of $90\text{--}370$ mrad for HAADF and $11\text{--}23$ mrad for ABF images. The XPS measurements were performed using PHI-5400 equipment with Al K α beam source (250 W) and a position-sensitive detector (PSD) was used to determine the surface composition of the materials. The Fourier transform infrared spectroscopy-Raman spectroscopy was carried with a confocal Raman microscope (Horiba HR Evolution), equipped with a diode laser emitting at 532 nm. The nominal laser power was filtered down to 1 mW to avoid sample overheating. Spectra were recorded with the accumulation time of 60 s.

DFT studies. All the density functional theory (DFT) calculations were performed by Vienna Ab-initio Simulation Package^{65,66} (VASP), employing the Projected Augmented Wave⁶⁷ (PAW) method. The revised Perdew-Burke-Ernzerhof (RPBE) functional was used to describe the exchange and correlation effects.⁶⁸⁻⁷⁰ The GGA + U calculations are performed using the model proposed by Dudarev et al.⁷¹, with the U_{eff} ($U_{\text{eff}} = \text{Coulomb } U - \text{exchange } J$) values of 3.3 eV and 4 eV for Co and Fe, respectively. For all the geometry optimizations, the cutoff energy was set to be 500 eV. A $3 \times 3 \times 1$ Monkhorst-Pack grids⁷² was used to carry out the surface calculations on the (111) surface of CoFe_2O_4 . At least 20 \AA vacuum layer was applied in z-direction of the slab models, preventing the vertical interactions between slabs.

In alkaline conditions, OER could occur in the following four elementary steps:



where * denotes the active sites on the catalyst surface. Based on the above mechanism, the free energy of three intermediate states, *OH, *O, and *OOH, are important to identify a given material's OER activity. The computational hydrogen electrode (CHE) model⁷³ was used to calculate the free energies of OER, based on which the free energy of an adsorbed species is defined as

$$\Delta G_{\text{ads}} = \Delta E_{\text{ads}} + \Delta E_{\text{ZPE}} - T\Delta S_{\text{ads}} \quad (6)$$

where ΔE_{ads} is the electronic adsorption energy, ΔE_{ZPE} is the zero point energy

difference between adsorbed and gaseous species, and $T\Delta S_{\text{ads}}$ is the corresponding entropy difference between these two states. The electronic binding energy is referenced as $\frac{1}{2} \text{H}_2$ for each H atom, and $(\text{H}_2\text{O} - \text{H}_2)$ for each O atom, plus the energy of the clean slab. The corrections of zero point energy and entropy of the OER intermediates can be found in the Supplementary Table 2.

Data availability

The data that support the findings of this study are available from the corresponding author upon reasonable request.

Received: 1 September 2020; Accepted: 2 April 2021;

Published online: 10 May 2021

References

- Young, J. L. et al. Direct solar-to-hydrogen conversion via inverted metamorphic multi-junction semiconductor architectures. *Nat. Energy* **2**, 17028 (2017).
- Aurbach, D., McCloskey, B. D., Nazar, L. F. & Bruce, P. G. Advances in understanding mechanisms underpinning lithium-air batteries. *Nat. Energy* **1**, 16128 (2016).
- Duan, C. et al. Highly durable, coking and sulfur tolerant, fuel-flexible protonic ceramic fuel cells. *Nature* **557**, 217–222 (2018).
- Cheng, W. et al. Lattice-strained metal-organic-framework arrays for bifunctional oxygen electrocatalysis. *Nat. Energy* **4**, 115–122 (2019).
- Koshikawa, H. et al. Single nanometer-sized NiFe-layered double hydroxides as anode catalyst in anion exchange membrane water electrolysis cell with energy conversion efficiency of 74.7% at 1.0 A/ cm^2 . *ACS Catal.* **10**, 1886–1893 (2020).
- Stoerzinger, K. A., Qiao, L., Biegalski, M. D. & Shao-Horn, Y. Orientation-dependent oxygen evolution activities of rutile IrO_2 and RuO_2 . *J. Phys. Chem. Lett.* **5**, 1636–1641 (2014).
- Hong, W. T. et al. Toward the rational design of non-precious transition metal oxides for oxygen electrocatalysis. *Energy Environ. Sci.* **8**, 1404–1427 (2015).
- Calle-Vallejo, F. et al. Number of outer electrons as descriptor for adsorption processes on transition metals and their oxides. *Chem. Sci.* **4**, 1245–1249 (2013).
- Man, I. C. et al. Universality in oxygen evolution electrocatalysis on oxide surfaces. *ChemCatChem* **3**, 1159–1165 (2011).
- Suntivich, J., May, K. J., Gasteiger, H. A., Goodenough, J. B. & Shao-Horn, Y. A perovskite oxide optimized for oxygen evolution catalysis from molecular orbital principles. *Science* **334**, 1383–1385 (2011).
- Chao, W. et al. Cations in octahedral sites: a descriptor for oxygen electrocatalysis on transition-metal spinels. *Adv. Mater.* **29**, 1606800 (2017).
- Suntivich, J. et al. Design principles for oxygen-reduction activity on perovskite oxide catalysts for fuel cells and metal-air batteries. *Nat. Chem.* **3**, 546–550 (2011).
- Lim, T., Hans, J. W. & Gracia, J. Layered antiferromagnetic ordering in the most active perovskite catalysts for the oxygen evolution reaction. *ChemCatChem* **8**, 2968–2974 (2016).
- Sharpe, R. et al. Orbital physics of perovskites for the oxygen evolution reaction. *Top. Catal.* **61**, 267–275 (2018).
- Sharpe, R., Lim, T., Jiao, Y., Niemantsverdriet, J. W. H. & Gracia, J. Oxygen evolution reaction on perovskite electrocatalysts with localized spins and orbital rotation symmetry. *ChemCatChem* **8**, 3762–3768 (2016).
- Gracia, J. et al. Analysis of the magnetic entropy in oxygen reduction reactions catalysed by manganite perovskites. *ChemCatChem* **9**, 3358–3363 (2017).
- Chretien, S. & Metiu, H. O_2 evolution on a clean partially reduced rutile TiO_2 (110) surface and on the same surface precovered with Au1 and Au2: the importance of spin conservation. *J. Chem. Phys.* **129**, 074705 (2008).
- Torun, E., Fang, C. M., de Wijs, G. A. & de Groot, R. A. Role of magnetism in catalysis: RuO_2 (110) surface. *J. Phys. Chem. C* **117**, 6353–6357 (2013).
- Nazmutdinov, R. R., Santos, E. & Schmickler, W. Spin effects in oxygen electrocatalysis: a discussion. *Electrochem. Commun.* **33**, 14–17 (2013).
- Ramos, A. V., Santos, T. S., Miao, G. X., Guittet, M.-J., Moussy, J.-B. & Moodera, J. S. Influence of oxidation on the spin-filtering properties of CoFe_2O_4 and the resultant spin polarization. *Phys. Rev. B* **78**, 180402 (2008).
- Zhi-Min, Liao et al. Spin-filter effect in magnetite nanowire. *Nano Lett.* **6**, 1087–1091 (2006).
- Gracia, J. Itinerant spins and bond lengths in oxide electrocatalysts for oxygen evolution and reduction reactions. *J. Phys. Chem. C* **123**, 9967–9972 (2019).
- Gracia, J., Sharpe, R. & Munarriz, J. Principles determining the activity of magnetic oxides for electron transfer reactions. *J. Catal.* **361**, 331–338 (2018).

24. Gracia, J. Spin dependent interactions catalyse the oxygen electrochemistry. *Phys. Chem. Chem. Phys.* **19**, 20451–20456 (2017).
25. Mtangi, W. et al. Control of electrons' spin eliminates hydrogen peroxide formation during water splitting. *J. Am. Chem. Soc.* **139**, 2794–2798 (2017).
26. Zhang, W., Banerjee-Ghosh, K., Tassinari, F. & Naaman, R. Enhanced electrochemical water splitting with chiral molecule-coated Fe₃O₄ nanoparticles. *ACS Energy Lett.* **3**, 2308–2313 (2018).
27. Mondal, P. C., Fontanesi, C., Waldeck, D. H. & Naaman, R. Spin-dependent transport through chiral molecules studied by spin-dependent electrochemistry. *Acc. Chem. Res.* **49**, 2560–2568 (2016).
28. Jiao, Y., Sharpe, R., Lim, T., Niemantsverdriet, J. W. H. & Gracia, J. Photosystem II acts as a spin-controlled electron gate during oxygen formation and evolution. *J. Am. Chem. Soc.* **139**, 16604–16608 (2017).
29. Lüders, U. et al. Spin filtering through ferrimagnetic NiFe₂O₄ tunnel barriers. *Appl. Phys. Lett.* **88**, 082505 (2006).
30. Garcés-Pineda, F. A., Blasco-Ahicart, M., Nieto-Castro, D., López, N. & Galán-Mascarós, J. R. Direct magnetic enhancement of electrocatalytic water oxidation in alkaline media. *Nat. Energy* **4**, 519–525 (2019).
31. Yang, Y., Grant, K. M., Henry, S. W. & Chen, S. Magnetochemistry of nitrothiophenolate-functionalized gold nanoparticles. *Langmuir* **19**, 9446–9449 (2003).
32. Monzon, L. M. A. & Coey, J. M. D. Magnetic fields in electrochemistry: The Kelvin force. A mini-review. *Electrochem. Commun.* **42**, 42–45 (2014).
33. Monzon, L. M. A. & Coey, J. M. D. Magnetic fields in electrochemistry: The Lorentz force. A mini-review. *Electrochem. Commun.* **42**, 38–41 (2014).
34. Olivier Devos, O. A. Jean-Paul Chopart, and Alain Olivier is there a magnetic field effect on electrochemical kinetics? *J. Phys. Chem. A* **104**, 1544–1548 (2000).
35. Gatard, V., Deseure, J. & Chatenet, M. Use of magnetic fields in electrochemistry: a selected review. *Curr. Opin. Electrochem.* **23**, 96–105 (2020).
36. Monzon, L. M. A., Nair, V., Reilly, B. & Coey, J. M. D. Magnetically-induced flow during electropolishing. *J. Electrochem. Soc.* **165**, E679–E684 (2018).
37. Miyake, T. & Rolandi, M. Grothuss mechanisms: from proton transport in proton wires to bioprotonic devices. *J. Phys. Condens Matter* **28**, 023001 (2016).
38. Chappert, C., Fert, A. & Van Dau, F. N. The emergence of spin electronics in data storage. *Nat. Mater.* **6**, 813–823 (2007).
39. Binash, G., Grunberg, P., Saurenbach, F. & Zinn, W. Enhanced magnetoresistance in layered magnetic structures with antiferromagnetic interlayer exchange. *Phys. Rev. B Condens Matter* **39**, 4828–4830 (1989).
40. Zhou, B. H. & Rinehart, J. D. A size threshold for enhanced magnetoresistance in colloidal prepared CoFe₂O₄ nanoparticle solids. *ACS Cent. Sci.* **4**, 1222–1227 (2018).
41. Chen, J. et al. Murray bistable magnetoresistance switching in exchange-coupled CoFe₂O₄-Fe₃O₄ binary nanocrystal superlattices by self-assembly and thermal annealing. *ACS Nano* **7**, 1478–1486 (2013).
42. Gul, I. H. & Maqsood, A. Structural, magnetic and electrical properties of cobalt ferrites prepared by the sol-gel route. *J. Alloy. Compd.* **465**, 227–231 (2008).
43. Xu, Z. J. From two-phase to three-phase: the new electrochemical interface by oxide electrocatalysts. *Nanomicro Lett.* **10**, 8 (2018).
44. Xu, Z. J. Transition metal oxides for water oxidation: all about oxyhydroxides? *Sci. China Mater.* **63**, 3–7 (2019).
45. Wu, T. et al. Iron-facilitated dynamic active-site generation on spinel CoAl₂O₄ with self-termination of surface reconstruction for water oxidation. *Nat. Catal.* **2**, 763–772 (2019).
46. Chen, Y. et al. Exceptionally active iridium evolved from a pseudo-cubic perovskite for oxygen evolution in acid. *Nat. Commun.* **10**, 572–582 (2019).
47. El Arrassi, A. et al. Intrinsic activity of oxygen evolution catalysts probed at single CoFe₂O₄ nanoparticles. *J. Am. Chem. Soc.* **141**, 9197–9201 (2019).
48. Chandramohan, P., Srinivasan, M. P., Velmurugan, S. & Narasimhan, S. V. Cation distribution and particle size effect on Raman spectrum of CoFe₂O₄. *J. Solid State Chem.* **184**, 89–96 (2011).
49. Zhou, Z. et al. Electronic structure studies of the spinel CoFe₂O₄ by X-ray photoelectron spectroscopy. *Appl. Surf. Sci.* **254**, 6972–6975 (2008).
50. Fang, Y.-H. & Liu, Z.-P. Tafel kinetics of electrocatalytic reactions: from experiment to first-principles. *ACS Catal.* **4**, 4364–4376 (2014).
51. Sun, S. et al. Switch of the rate-determining step of water oxidation by spin-selected electron transfer in spinel oxides. *Chem. Mater.* **31**, 8106–8111 (2019).
52. Duan, Y. et al. Revealing the impact of electrolyte composition for co-based water oxidation catalysts by the study of reaction kinetics parameters. *ACS Catal.* **10**, 4160–4170 (2020).
53. Craig, M. J. et al. Universal scaling relations for the rational design of molecular water oxidation catalysts with near-zero overpotential. *Nat. Commun.* **10**, 4993 (2019).
54. Garcia-Melchor, M., Vilella, L., López, N. & Vojvodic, A. Computationally probing the performance of hybrid, heterogeneous, and homogeneous iridium-based catalysts for water oxidation. *ChemCatChem* **8**, 1792–1798 (2016).
55. Wei, C. et al. Cations in octahedral sites: a descriptor for oxygen electrocatalysis on transition-metal spinels. *Adv. Mater.* **29**, 1606800 (2017).
56. Teillet, J., Bouere, F. & Krishnan, R. Magnetic structure of CoFe₂O₄. *J. Magn. Magn. Mater.* **123**, 93–96 (1993).
57. Guillot, M., Ostorero, J. & Marchand, A. High magnetic field magnetization study in cadmium-cobalt ferrite single crystals. *Condens. Matter Phys.* **71**, 193–197 (1988).
58. Shin, Y. et al. Alleviating oxygen evolution from Li-excess oxide materials through theory-guided surface protection. *Nat. Commun.* **9**, 4597 (2018).
59. Zhang, L., Cheruvathur, A., Biz, C., Fianchini, M. & Gracia, J. Ferromagnetic ligand holes in cobalt perovskite electrocatalysts as an essential factor for high activity towards oxygen evolution. *Phys. Chem. Chem. Phys.* **21**, 2977–2983 (2019).
60. Chen, L. D. et al. Understanding the apparent fractional charge of protons in the aqueous electrochemical double layer. *Nat. Commun.* **9**, 3202 (2018).
61. Yang, C. et al. Cation insertion to break the activity/stability relationship for highly active oxygen evolution reaction catalyst. *Nat. Commun.* **11**, 1378 (2020).
62. Dionigi, F. et al. In-situ structure and catalytic mechanism of NiFe and CoFe layered double hydroxides during oxygen evolution. *Nat. Commun.* **11**, 2522 (2020).
63. Suntivich, J., Gasteiger, H. A., Yabuuchi, N. & Shao-Horn, Y. Electrocatalytic measurement methodology of oxide catalysts using a thin-film rotating disk electrode. *J. Electrochem. Soc.* **157**, B1263–B1268 (2010).
64. Sun, S., Zhou, Y., Hu, B., Zhang, Q. & Xu, Z. J. Ethylene glycol and ethanol oxidation on spinel Ni-Co oxides in alkaline. *J. Electrochem. Soc.* **163**, H99–H104 (2015).
65. Kresse, G. & Furthmüller, J. Efficient iterative schemes for ab initio total-energy calculations using a plane-wave basis set. *Phys. Rev. B* **54**, 11169–11186 (1996).
66. Kresse, G. & Hafner, J. Ab initio molecular dynamics for liquid metals. *Phys. Rev. B* **49**, 14251–14269 (1994).
67. Blöchl, P. E. Projector augmented-wave method. *Phys. Rev. B* **50**, 17953–17979 (1994).
68. Perdew, J. P., Burke, K. & Ernzerhof, M. Generalized gradient approximation made simple. *Phys. Rev. Lett.* **77**, 3865–3868 (1996).
69. Zhang, Y. & Yang, W. Comment on “Generalized Gradient Approximation Made Simple”. *Phys. Rev. Lett.* **80**, 890 (1998).
70. Hammer, B., Hansen, L. B. & Nørskov, J. K. Improved adsorption energetics within density-functional theory using revised Perdew-Burke-Ernzerhof functionals. *Phys. Rev. B* **59**, 7413–7421 (1999).
71. Dudarev, S., Botton, G., Savrasov, S., Humphreys, C. & Sutton, A. Electron-energy-loss spectra and the structural stability of nickel oxide: An LSDA+ U study. *Phys. Rev. B* **57**, 1505 (1998).
72. Monkhorst, H. J. & Pack, J. D. Special points for Brillouin-zone integrations. *Phys. Rev. B* **13**, 5188 (1976).
73. Nørskov, J. K. et al. Origin of the overpotential for oxygen reduction at a fuel-cell cathode. *J. Phys. Chem. B* **108**, 17886–17892 (2004).

Acknowledgements

We thank the support from the National Nature Science Foundation of China (Grant No. 11274370 and 51471185) and the National National Key R&D Program of China (Grant No. 2016YFJC020013 and 2018FYA0305800). Authors in Singapore thank the support from the Singapore Ministry of Education Tier 2 Grants (MOE2017-T2-1-009 and MOE2018-T2-2-027) and the Singapore National Research Foundation under its Campus for Research Excellence and Technological Enterprise (CREATE) programme. We appreciate the Facility for Analysis, Characterisation, Testing, and Simulation (FACTS) at Nanyang Technological University for materials characterizations. This work was supported by the National Research Foundation (NRF), Prime Minister's Office, Singapore under its Campus for Research Excellence and Technological Enterprise (CREATE) programme through the eCO2EP project operated by the Cambridge Centre for Advanced Research and Education in Singapore (CARES) and the Berkeley Educational Alliance for Research in Singapore (CARES).

Author contributions

X.R., T.W., and Y.S. contribute equally to this work. Z.X., X.R., and T.W. conceived the original concept and designed the experiments. T.W. prepared the materials. X.R.

performed most characterizations and analysis. G.X. and X.R. performed the Raman spectroscopy measurement. H.Y., X.R., and Y.L. carried out magnetic property measurements and analysis. Y.S. contributed the DFT calculations and analysis. T.W., X.R., H.Y., H.G., and Z.X. contributed the mechanism analysis. J.G. contributed the explanation of QSEI theory. X.R., T.W., Y.S., H.Y., X.L., C.S., H.G., and Z.X. wrote the manuscript with the input from all authors. All authors engaged in the analysis of experimental results and manuscript edition.

Competing interests

The authors declare no competing interests.

Additional information

Supplementary information The online version contains supplementary material available at <https://doi.org/10.1038/s41467-021-22865-y>.

Correspondence and requests for materials should be addressed to H.Y. or Z.J.X.

Peer review information *Nature Communications* thanks Jonathan Deseure, Ron Naaman, and other, anonymous, reviewers for their contributions to the peer review of this work. Peer review reports are available.

Reprints and permission information is available at <http://www.nature.com/reprints>

Publisher's note Springer Nature remains neutral with regard to jurisdictional claims in published maps and institutional affiliations.



Open Access This article is licensed under a Creative Commons Attribution 4.0 International License, which permits use, sharing, adaptation, distribution and reproduction in any medium or format, as long as you give appropriate credit to the original author(s) and the source, provide a link to the Creative Commons license, and indicate if changes were made. The images or other third party material in this article are included in the article's Creative Commons license, unless indicated otherwise in a credit line to the material. If material is not included in the article's Creative Commons license and your intended use is not permitted by statutory regulation or exceeds the permitted use, you will need to obtain permission directly from the copyright holder. To view a copy of this license, visit <http://creativecommons.org/licenses/by/4.0/>.

© The Author(s) 2021